ACS OMEGA

http://pubs.acs.org/journal/acsodf

Article

# $WS_2$-Nanosheet-Modified Electrodes as an Efficient Electrochemical Sensing Platform for the Nonenzymatic Detection of the Insecticide Imidacloprid

V. S. Haritha, S. R. Sarath Kumar,* and R. B. Rakhi*

Cite This: *ACS Omega* 2023, 8, 8695−8702

Read Online

ACCESS | Metrics & More | Article Recommendations

**ABSTRACT:** Imidacloprid (IMI) is a systemic insecticide, which is widely used for seed treatment and pest control in vegetables. The unwarranted presence of traces of IMI in vegetables and groundwater is a matter of grave concern which needs to be detected and quantified in order to effect remedial measures for the sake of food safety. In this work, we communicate the fabrication of tungsten sulfide ($WS_2$) nanosheets and the construction of an amperometric sensor for the precise determination of IMI. The sensor performances were evaluated by using cyclic voltammetry (CV). The presence of surface-active sites and the fast electron transfer on $WS_2$/GCE favored the electrochemical reduction of the aromatic nitro group in IMI. The developed IMI sensor displayed a linear range of IMI detection from 10 to 90 $\mu$M with a detection limit of 0.28 $\mu$M. The developed $WS_2$/GCE sensor also displayed good sensitivity, with a value of 3.98 $\mu$A $\mu M^{-1}$ $cm^{-2}$. The electrochemical measurements demonstrated the superior selectivity of the constructed $WS_2$/GCE sensor for IMI detection, which makes it suitable for practical applications.

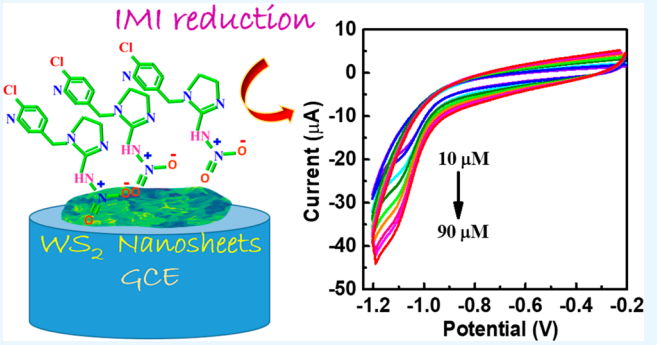


## INTRODUCTION

The perpetual increase in population has continuously raised the demand for food and crop production across many countries.[1] Pesticides are well-known chemical entities that play a vital role in boosting agricultural productivity by effectively protecting crops from pests and thereby enhancing crop yield.[2] Neonicotinoids are one of the extensively used classes of agrochemicals, which are globally registered for use in more than 120 countries, as they exhibit high potency against various insects.[3−5] The typical representatives of this agrochemical class irreversibly bind the nicotinic acetylcholine receptors, which are essential for the appropriate functioning of the central nervous system of insects. This hinders neural transmission, leading to paralysis and ultimately the death of insects.[6,7]

Imidacloprid (IMI) is one of the most commonly and commercially used neonicotinoid-based insecticides for repelling pests from more than 140 crops, including rice, cotton, and vegetables.[5,8] It offers high efficiency, specificity and a broad spectrum with fewer toxic effects for mammals.[9] Nevertheless, considering their physicochemical properties such as high solubility in water, good stability, long half-life in soil and water, and resistance to hydrolysis, it has a greater capability to encroach in groundwater resources.[10,11] The intensive and widespread use of IMI in the agricultural sector has increased its persistence in environmental resources, leading to pollution in soil and water, and subsequently it has invaded the food chain.[12,13] Furthermore, the overuse of IMI has elevated the limit of IMI residues in agricultural products, which is consequently creating ill effects (neurological disorders, genotoxicity, etc.) in consumers.[14,15] Thus, countries like China and Japan have introduced a maximum residual limit of IMI in brown rice as 0.05 and 1 mg/kg, respectively.[5] Therefore, this mandates intensive and robust procedures to monitor and detect IMI residues from environmental resources and agricultural products. Conventional chromatographic methods are commonly employed for the estimation of IMI residues. Although chromatography offers good reproducibility and accuracy, it requires complex sample preparation, skilled technicians, and sophisticated instruments, which make the analysis time-consuming and expensive.[6,16,17]

Received: December 20, 2022
Accepted: February 13, 2023
Published: February 24, 2023





https://doi.org/10.1021/acsomega.2c08077
*ACS Omega* 2023, 8, 8695−8702

In comparison with the traditional methods of detection, an electrochemical sensing platform appears to be a potential alternative for monitoring IMI residues with high selectivity and sensitivity, fast response, and affordable practical cost.[18,19] The selection of the appropriate electrode materials is one of the fundamental aspects of electrochemical sensors.[20] The sensing performance of the electrochemical biosensors is heavily dependent on the nature and properties of the sensor/electrode materials. On consideration of the sensor/electrode material requirements, nanomaterials have been given a greater preference due to their unique properties, which result from the quantum confinement effect and the rich surface chemistry.[21,22] Among various nanomaterials, 2D nanomaterials have exotic physical, chemical, electronic and optical properties.[23] For instance, concerning the thickness and composition of the 2D nanomaterials, the electronic properties vary from metallic/semimetallic to semiconducting and insulating.[24]

2D materials have received greater attention in the field of electrochemical biosensing ever since the discovery of graphene. Graphene and its composites with metal nanostructures and polymers have been reported to be excellent sensor materials for the detection and quantification of IMI.[25−28] However, other classes of 2D materials such as transition-metal dichalcogenides (TMDs) have remained less examined as transducers in the electrochemical sensing of IMI. TMDs are the inorganic analogues of graphene, having exciting applications in a wide variety of fields such as electronics, optoelectronics, catalysis, and biosensors.[29−31] Among TMDs, $MoS_2$ is generally accepted for biosensing applications, but others like $WS_2$,, which share a similar structure but offer unique optical and electronic properties, remain comparatively less investigated. The typical $WS_2$ nanostructures have exceptional optical and electronic properties with superior electrical conductivity, and this property can be tuned by manipulating the crystal structure and the number of layers. Moreover, the 2D layered $WS_2$ also displays a high surface area, which further leads to an abundance of active sites, which fundamentally enhances the catalytic activity. It is also a nontoxic material, which is resistant to corrosion and is inexpensive.[32,33] In this study, a facile hydrothermal route was developed for the synthesis of $WS_2$ nanosheets (shown in Figure 1), and a novel electrochemical sensor was fabricated by incorporating $WS_2$-modified glassy-carbon electrodes for the detection and quantification of the insecticide imidacloprid.

## RESULTS AND DISCUSSION

XRD measurements were done to identify the component structure and the phase purity of the as-prepared sample. Figure 2a depicts the XRD pattern of the as-prepared sample. The dominant peaks observed can be indexed to the crystal planes of the hexagonal phase of $WS_2$ with a space group of $P6_3/mmc$ (No. 194) matching with the JCPDS card number 08-0237. The highly intense peak at (002) represents the periodicity in the *c* axis and the construction of stacked layered $WS_2$.[34] The high intensity of peaks and their broad nature indicate the nanocrystalline nature of the sample.

To further characterize the as-prepared sample, Raman spectroscopy was employed. Figure 2b shows the Raman spectrum of the as-prepared powder. From the Raman spectra, we observe two active Raman modes: $E^1_{2g}$ at ∼349.9 $cm^{-1}$ and $A_{1g}$ at ∼413.7 $cm^{-1}$. $E^1_{2g}$ at 349.9 $cm^{-1}$ corresponds to the in-plane vibrational mode and $A_{1g}$ at 413.7 $cm^{-1}$ represents the

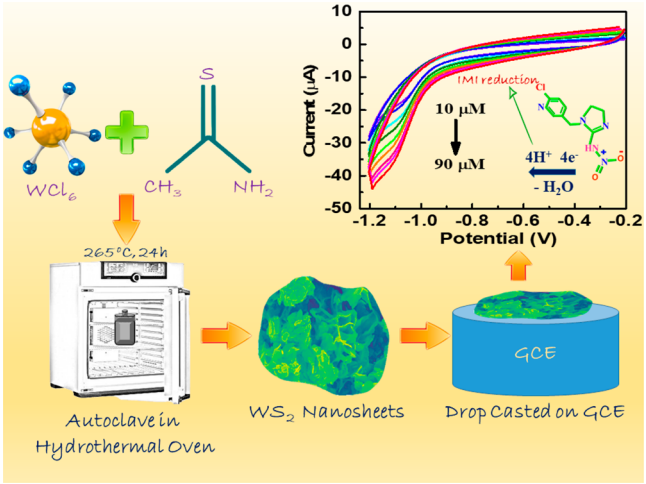


**Figure 1.** Fabrication of $WS_2$/GCE for IMI detection.

out-of-plane vibrational mode. This further confirms the formation of $WS_2$, and no other vibrational modes from $WO_3$ were observed in the Raman spectrum. By calculating the intensity ratios ($A_{1g}/E^1_{2g}$) and the frequency differences (between $E^1_{2g}$ and $A_{1g}$), the number of layers can be estimated.[35] An intensity ratio of 1.1 and a difference in frequency of 63.8 $cm^{-1}$ indicate the construction of few-layered $WS_2$ nanosheets. The high-resolution XPS spectra were analyzed to determine the oxidation states of the prepared compound. As shown in Figure 2c, the spectrum of W could be deconvoluted into four peaks; the two prominent peaks at 32.4 and 34.6 eV attributed to $W^{4+}$ respectively correspond to the W $4f_{7/2}$ and W $4f_{5/2}$ orbitals, indicating the formation of $WS_2$. The two relatively lesser-intensity high-energy peaks at 35.5 and 38.0 eV are from $WO_3$ (oxidation state of +6), corresponding to the high- and low-energy orbitals, respectively. The high-resolution XPS spectrum of S 2p (shown in Figure 2d) has two broad peaks at 162.2 eV (S $2p_{3/2}$ peak attributed to $S^{2-}$) and 163.4 eV (S $2p_{1/2}$ peak attributed to $S^{2-}$). This is indicative of the formation of $WS_2$, and also there is no presence of $WS_3$ in the sample. Figure 2e represents the nitrogen adsorption/desorption isotherm of $WS_2$ nanosheets. A standard type IV isotherm with evident hysteresis loops is identified, which is the general characteristic of mesoporosity. The estimated pore diameter of the sample was ∼7.2 nm, which matches the mesoporous materials. The as-prepared $WS_2$ nanostructures also have a BET surface area of 9.18 $m^2/g$. Figure 2f represents the BJH pore size distribution plot of $WS_2$ nanosheets. The calculated total pore volume of the as-prepared sample is $1.67 \times 10^{-2}$ $cm^3/g$. The morphological and structural characterizations were also done by using electron microscopy techniques. The low-magnification and high-magnification FESEM images of the powder samples are shown in Figure 3a,b, respectively. They display a large number of uniformly distributed and differently oriented nanosheets of $WS_2$. Figure 3c depicts the bright-field TEM image of the sample. TEM analysis further substantiates the formation of nanosheets of $WS_2$.

Figure 3d shows the HRTEM image of a nanosheet with a resolved interplanar spacing of 0.31 nm, which matches with the (004) (shown as the inset of Figure 3d) characteristic reflection of the 2H phase of $WS_2$. The nanosheet-like morphology is confirmed by the FESEM and TEM analysis.


https://doi.org/10.1021/acsomega.2c08077
ACS Omega 2023, 8, 8695−8702

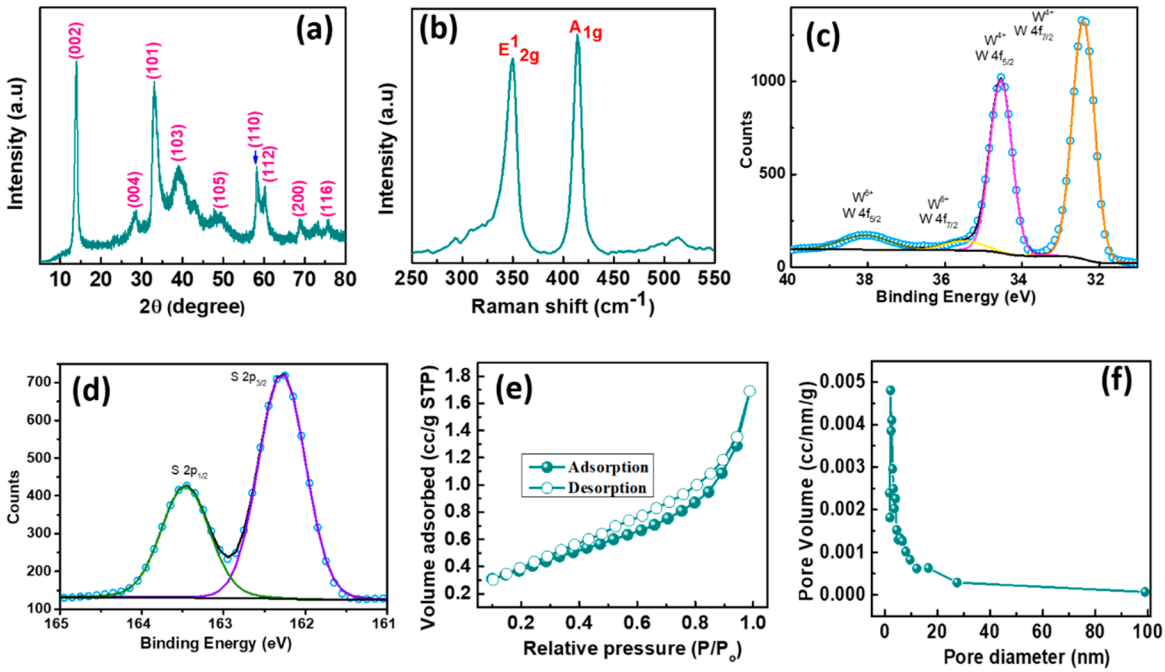


**Figure 2.** (a) PXRD and (b) Raman spectra of $WS_2$. (c) High-resolution XPS spectra of W 4f and (d) S 2p in $WS_2$. (e) BET isotherm and (f) BJH pore size distribution plot of the prepared sample.

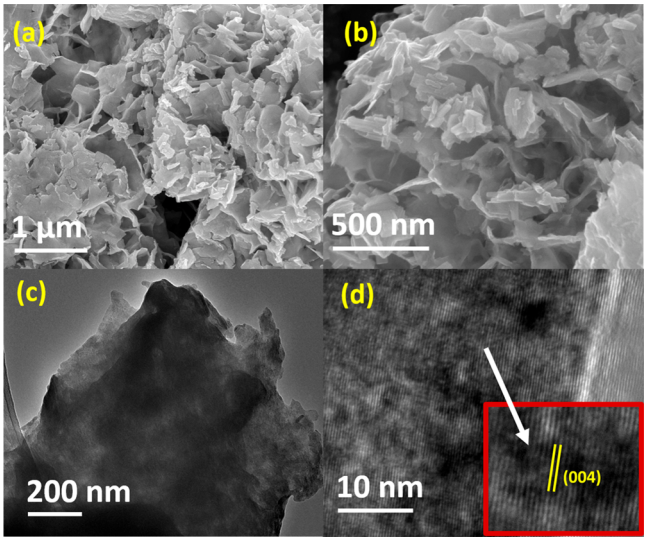


**Figure 3.** (a, b) FESEM images of the as-prepared sample. (c) Bright-field TEM image and (d) HRTEM image of $WS_2$.

**Electrochemical Studies.** The electrochemical changes on bare GCE and $WS_2$-nanosheet-modified electrodes were studied using electrochemical impedance spectroscopy (EIS) with the help of a 5 mmol/L $[Fe(CN)_6]^{3-/4-}$ redox probe containing 0.1 mol/L KCl supporting electrolyte solution. Figure 4a depicts the EIS plots of bare GCE and $WS_2$/GCE, Figure 4b represents the fitted Nyquist plot of $WS_2$/GCE, and Figure 4c shows the equivalent circuit used for fitting the Nyquist plot.[36] Generally, all Nyquist/EIS plots include a semicircular region accompanied by a linear region. The former corresponds to the charge-transfer-limited processes and the latter is ascribed to the diffusion-limited processes. The values of charge-transfer resistance ($R_{ct}$) and solution resistance ($R_s$) were obtained from the diameter of the semicircular region and the $X$-intercept values. $R_{ct}$ and $R_s$ values of bare GCE and $WS_2$/GCE were estimated as 122.28, 3.36 Ω and 2.72, 2.65 Ω respectively. A lower $R_{ct}$ value of 3.36 Ω validates the faster electron transfer mechanism on the $WS_2$/GCE−electrolyte interface in comparison with the bare GCE.

The electrochemical properties of modified and unmodified electrodes were studied by using CV. Figure 4d shows the cyclic voltammograms of bare GCE and $WS_2$/GCE in the $[Fe(CN)_6]^{3-/4-}$ redox probe at a scan rate of 50 mV/s. Both bare and modified electrodes displayed distinct redox peaks, corresponding to the oxidation and reduction processes. As compared to bare GCE, enhanced peak currents were observed for $WS_2$-modified electrodes. This indicates that the assimilation of $WS_2$ on GCE stimulates electron transfer to the $[Fe(CN)_6]^{3-/4-}$ probe. This further highlights the catalytic ability and conductivity of $WS_2$ nanosheets. Figure 4e represents the cyclic voltammograms of $WS_2$/GCE at various scan rates ranging from 50 to 450 mV/s, and Figure 4f shows the linear plots of anodic peak currents versus the square root of the scan rate. The electrochemically active surface area of $WS_2$/GCE is calculated using the Randles−Sevcik equation (1).[37]

$$I_p = 2.69 \times 10^5 n^{3/2} A D^{1/2} C \upsilon^{1/2} \quad (1)$$

$I_p$ is the peak current, $n$ the number of electrons transferred during the redox reactions (here $n$ = 1), $D$ is the diffusion coefficient ($7.60 \times 10^{-6}$ $cm^2/s$), and $C$ the concentration of the solution (5 mM); The slope of the linear plot (Figure 4d), $I_p/\upsilon^{1/2}$, is determined and substituted in eq 1, and the electroactive surface area ($A$) is calculated. The electrochemical active surface area of $WS_2$/GCE was estimated to be 0.2340 $cm^2$.

**Electrochemical Detection of IMI.** To investigate the electrochemical response of the insecticide IMI on the unmodified and $WS_2$-modified glassy-carbon electrodes, CV studies were conducted. CV curves were recorded in a potential window of −0.2 to −1.2 V. Figure 5a shows the


https://doi.org/10.1021/acsomega.2c08077
ACS Omega 2023, 8, 8695−8702

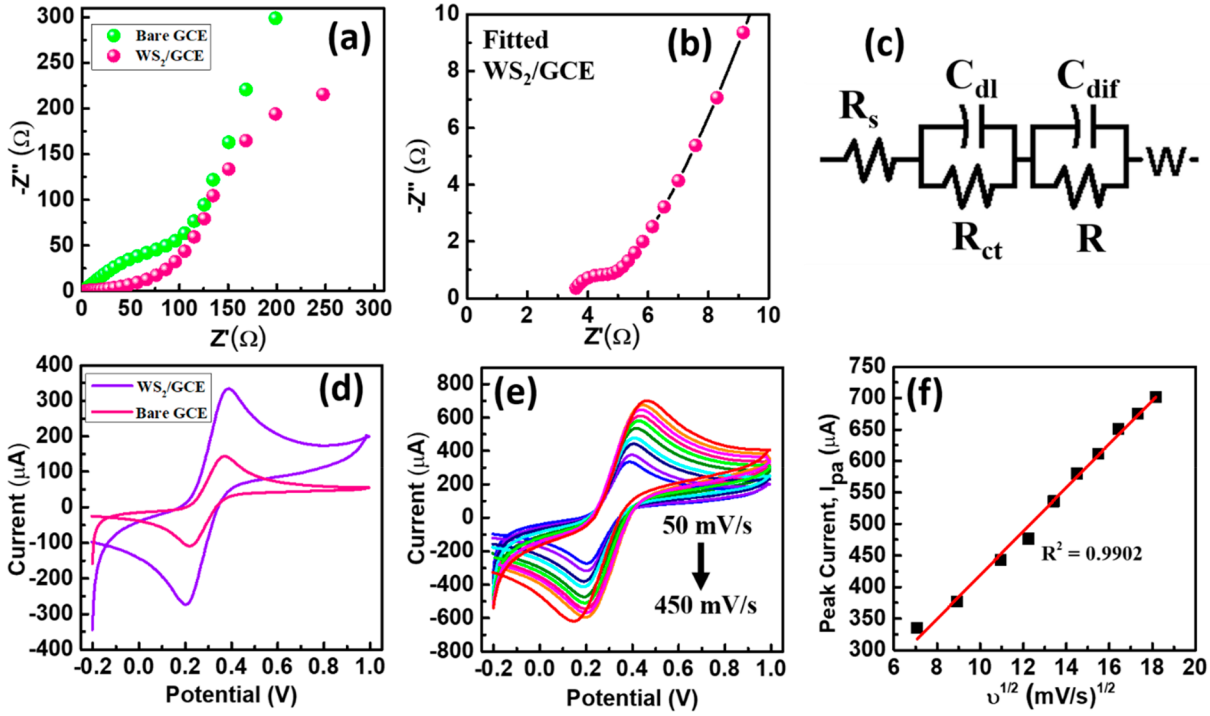


**Figure 4.** (a) Nyquist plots of unmodified GCE and $WS_2$-modified GCE in 5 mmol/L $[Fe(CN)_6]^{3-/4-}$ redox probe containing 0.1 mol/L KCl, (b) Fitted Nyquist plot of $WS_2$/GCE. (c) Equivalent circuit used for fitting the Nyquist plot, (d) CV curves of bare GCE and $WS_2$/GCE in 5 mmol/L $[Fe\ CN)_6]^{3-/4-}$ redox probe containing 0.1 mol/L KCl at a scan rate of 50 mV/s. (e) CV responses of $WS_2$-modified electrodes at different scan rates in 5 mmol/L $[Fe(CN)_6]^{3-/4-}$ redox probe. (f) Linear plot of anodic peak currents versus square root of scan rate.

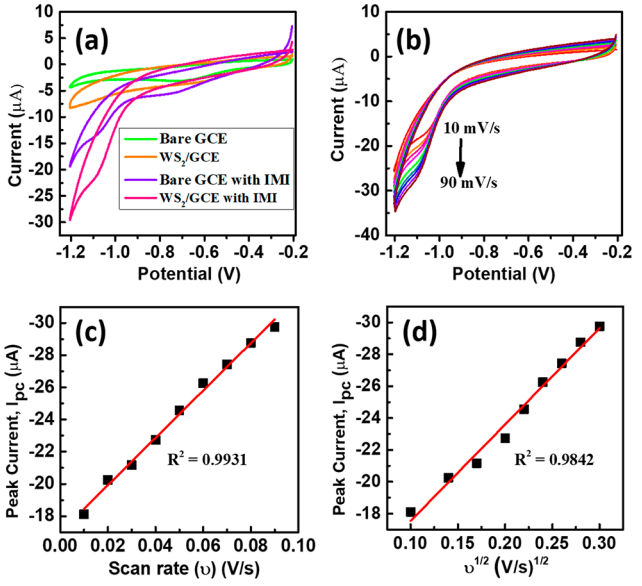


**Figure 5.** (a) Cyclic voltammograms of GCE and $WS_2$/GCE with 30 $\mu$M of IMI (violet and pink curves) and without IMI (green and orange). (b) Effect of scan rate and linear plots of $I_{pc}$ versus (c) $\upsilon$ and (d) $\upsilon^{1/2}$.

cyclic voltammograms of bare and $WS_2$-nanosheet-modified electrodes with 30 $\mu$M of IMI and without the addition of IMI for a scan rate of 50 mV/s in PBS having a concentration of 0.2 M and a pH value of 7. The absence of IMI does not generate any oxidation/reduction peaks in bare and modified electrodes (green and orange curves in Figure 5a). But in the presence of 30 $\mu$M of IMI, in the applied potential range, a weak irreversible cathodic reduction peak was observed for bare GCE at −1.09 V with a reduction peak current of −13.41 $\mu$A. In the case of $WS_2$-modified electrodes, an enhanced reduction peak at −1.07 V with a peak current of −21.58 $\mu$A was detected (violet and pink curves in Figure 5a). The feeble reduction peak on bare GCE indicates the absence of electroactive reaction sites on the unmodified electrodes. The remarkable enhancement in cathodic peak current on $WS_2$-nanosheet-modified electrodes correlates with the abundance of electroactive reaction sites on $WS_2$. This favors a fast electron transfer between IMI and the modified electrode surface, leading to the reduction of the electroactive nitro group ($-NO_2$) in IMI to the hydroxylamine (NHOH) group. The electrochemical reduction of IMI on $WS_2$/GCE is represented by eqs 2 and 3.

$$R{-}NO_2 + e^- \rightarrow R{-}NO_2^- \text{ (slow)} \quad (2)$$

$$R{-}NO_2 + 3e^- + 4H^+ \rightarrow R{-}NHOH + H_2O \text{ (fast)} \quad (3)$$

To further study the electron transfer kinetics in the electroreduction of IMI, cyclic voltammograms were recorded by varying scan rates from 10 to 90 mV/s. Figure 5b shows the cyclic voltammograms of 30 $\mu$M of IMI on $WS_2$-modified electrodes at different scan rates in 0.2 M PBS solution. For each scan rate, a well-defined cathodic peak was observed and the peak current continuously increased with an increase in scan rate. This implies that the electrocatalytic reduction of IMI is a kinetics-controlled process. The oxidation/reduction process on modified electrodes can progress through either adsorption or diffusion. Figure 5c,d depicts the linear relationships of $\upsilon$ and $\upsilon^{1/2}$ with peak currents. The correlation coefficients ($R^2$) obtained from the linear plots were 0.9931 and 0.9842, respectively. This validates that the cathodic peak currents of IMI manifest a scan rate dependence in comparison


https://doi.org/10.1021/acsomega.2c08077
ACS Omega 2023, 8, 8695−8702

with $\upsilon^{1/2}$. This confirms that the electrochemical reduction of IMI on $WS_2$-modified electrodes is an adsorption-controlled process. Generally, electroreduction of IMI involves two steps as shown in eqs 4 and 5.

$$\text{IMI (solution)} \rightarrow \text{IMI (adsorbed on electrode surface)} \quad (4)$$

$$\text{IMI (adsorbed on electrode surface)} + 4e \rightarrow \text{product} \quad (5)$$

Initially, the diffusion of IMI molecules takes place from the PBS solution to the electrode−electrolyte interface and then physisorption of IMI molecules occurs at the electrode surface. Step 2 is connected with an electron transfer reaction occurring between $WS_2$/GCE and IMI molecules. In the second step, the $NO_2$ group in IMI captures 4 electrons and transforms them into NHOH, represented in eqs 2 and 3. Equation 4 is considered to be the rate-determining step, and the kinetics in the electroreduction of IMI is controlled by adsorption. The Laviron approach was employed for determining the number of electrons transferred during the electroreduction of IMI. Figure 6a shows a linear diagram representing the relationship between cathodic peak potential ($E_{pc}$) and the natural logarithm of scan rate (ln $\upsilon$).

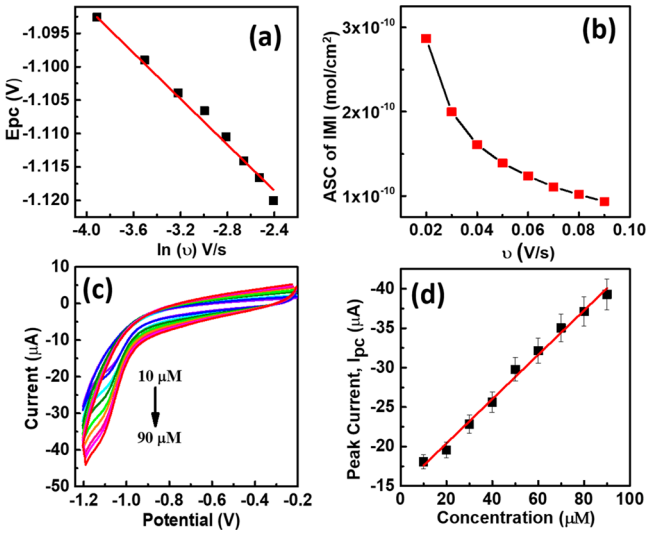


**Figure 6.** (a) Relationship between $E_{pc}$ and ln $\upsilon$. (b) Plot of ASC of IMI molecules versus scan rate. (c) Cyclic voltammograms of $WS_2$/GCE at varying IMI concentrations (10−90 $\mu$M). (d) Calibration plot of $I_{pc}$ versus concentration of IMI.

By employing Laviron approach, the slope of the linear plot is given by

$$\text{slope} = -RT/\alpha nF \quad (6)$$

By calculating the linear plot's slope, thenumber of electrons transferred ($n$) is estimated to be 3.97. This indicates that the electron transfer number during the reduction of the $-NO_2$ group in IMI to the NHOH group is 4, which agrees with the reduction process shown by eqs 2 and 3. The value of the charge transfer coefficient ($\alpha$) is taken as 0.5, $R$ is the universal gas constant, $F$ is the Faraday constant, and $T$ is the temperature. By employing the value of $n$, the adsorbed surface concentration (ASC) of IMI molecules on $WS_2$/GCE was calculated, and its relationship to the scan rate is shown in Figure 6b. The ASC of IMI molecules on $WS_2$/GCE for a scan rate of 50 mV/s was calculated to be $1.3902 \times 10^{-10}$ mol/cm$^2$.[38]

CV was used to determine the relationship between the concentration of IMI and the cathodic peak current values and to estimate the sensor parameters. Figure 6c represents the cyclic voltammograms of $WS_2$/GCE at varying concentrations of IMI ranging from 10 to 90 $\mu$M for a scan rate of 50 mV/s in the 0.2 M PBS electrolyte solution. From the CV curves, it was observed that, with an increase in IMI concentration, the cathodic reduction peak current also gradually increases. This again pinpoints the remarkable electrochemical activity of modified electrodes in the electroreduction of IMI. Beyond 90 $\mu$M the reduction peak current saturates. Figure 6d represents the linear calibration plots constructed by utilizing the CV curves at varying concentrations of IMI. From the linear plot, the sensor parameters like the limit of detection (LOD), sensitivity, and linear range of IMI detection can be estimated.

The LOD can be calculated by using the standard deviation value of the data and the slope of the calibration curve shown in Figure 6d.

Equation 7 is utilized for calculating LOD,

$$\text{LOD} = 3\sigma/M \quad (7)$$

where $\sigma$ is the standard deviation of 10 blank electrode response without the analyte and $M$ the slope of the calibration plot. The LOD of the proposed IMI sensor is calculated to be 0.28 $\mu$M. The sensitivity of the sensor ($S$) is calculated from the slope of the linear graph and the area of the conducting electrode surface using eq 8.

$$S = M/\text{area} \quad (8)$$

The calculated sensitivity of the $WS_2$/GCE IMI sensor is 3.98 $\mu$A $\mu$M$^{-1}$ cm$^{-2}$. The constructed sensor also advertised a linear range of IMI detection from 10 to 90 $\mu$M. The calculated parameters of the IMI sensor were correlated with those in the reported literature and are given in Table 1.

**Table 1. Comparative Study of Fabricated IMI Sensor Parameters with Those Reported in the Literature**

| method | modified electrode | LOD ($\mu$M) | detection range ($\mu$M) | ref |
|---|---|---|---|---|
| CV | PCz/CRGO/GCE | 0.22 | 3−10 | 39 |
| CV | GO/GCE | 0.36 | 0.8−10 | 40 |
| CV | AGCE | 0.61 | 4−20 | 41 |
| CV | imprinted-PoPD-RGO/GCE | 0.4 | 0.75−70 | 42 |
| CV | h-$MoO_3$HRs/GCE | 8.3 | 38.7−117 | 18 |
| CV | RGO/MnPc/GCE | 6.50 | 25−250 | 43 |
| CV | $WS_2$/GCE | 0.28 | 10−90 | this work |

For the practical utility of the IMI sensor, the specificity of the proposed sensor is extremely necessary. So, a study on the effect of various interfering compounds on the electrochemical response of IMI was done. The electrochemical behavior of $WS_2$/GCE with IMI and some of the probable interferents were studied using CV under optimized conditions. For the interference study, initially 50 $\mu$M of IMI was added to a PBS solution, and later 5-fold excess concentrations of various possible interferents like thiamethoxam (THI) (similar kind of pesticide), urea, common cations like $Mg^{2+}$ and $K^+$, heavy-metal cations like $Fe^{3+}$ and $Cu^{2+}$, common anions like $SO_4^{2-}$ and $Cl^-$ were added to the PBS solution. The respective CV


https://doi.org/10.1021/acsomega.2c08077
ACS Omega 2023, 8, 8695−8702

curves in the presence of interferents were recorded and are represented in Figure 7a. There were no additional peaks in

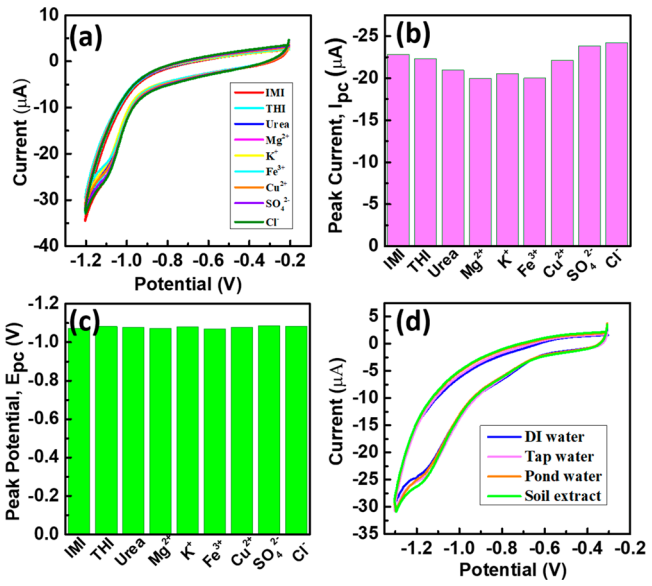


**Figure 7.** (a) Cyclic voltammograms of $WS_2$/GCE with 50 $\mu$M of IMI and other interfering compounds. Bar diagrams representing (b) peak current and (c) peak potential for interfering compounds like THI, urea, $Mg^{2+}$, $K^+$, $Fe^{3+}$, $Cu^{2+}$, $SO_4^{2-}$, and $Cl^-$. (d) CV curves of $WS_2$/GCE with the addition of 40 $\mu$M IMI in real samples.

the CV curves, which indicates the good selectivity of the fabricated IMI sensor. The bar diagrams of peak currents and peak potentials with different interferents are depicted in Figure 7b,c. Although there was a slight variation in peak currents when interferents were added, the change in peak potential values remained completely negligible. This further validates the high specificity of $WS_2$-modified electrodes in the quantification of IMI.

The stability and reproducibility of the proposed IMI sensor were examined using a CV analysis. To examine the reproducibility of $WS_2$/GCE for IMI detection, CV responses were recorded after storing the electrode in a desiccator for 10 days. A relative standard deviation of 1.49% reveals the excellent reproducibility of the sensor. After 10 days of storage, $WS_2$/GCE retained 80% of the current response. To recommend the fabricated $WS_2$/GCE−IMI sensor for practical applications, a real sample analysis is extremely crucial. For that, by adopting the standard addition method, 40 $\mu$M of IMI was added to water sources like DI water, tap water, pond water, and collected soil samples. The corresponding CV curves of the water samples and washed soil samples were recorded and are represented in Figure 7d. For all the samples, reduction peaks were observed, indicating the electrocatalytic reduction of IMI. IMI in real samples showed a recovery of greater than 90% with a %RSD of less than 2 (Table 2). This again highlights the practical applicability of the developed IMI sensor.

## CONCLUSION

$WS_2$ nanosheets were successfully produced through a facile hydrothermal route. An electrochemical sensor was fabricated by incorporating $WS_2$/GCE for the sensitive and selective detection of the insecticide IMI. The electrochemical performances were evaluated; $WS_2$/GCE exhibited an excellent

**Table 2. Recovery Studies from Real Samples**

| sample | %RSD | % recovery |
|---|---|---|
| DI water | 0.72 | 99.72 |
| pond water | 1.93 | 93.16 |
| tap water | 0.47 | 95.98 |
| soil extract | 0.61 | 95.71 |

electrocatalytic reduction of the aromatic nitro group in IMI to the corresponding hydroxylamine group. The obtained results depict that the reduction process was kinetically controlled by adsorption through a $4e^-$ transfer process. The fabricated sensor displayed a linear range of IMI detection from 10 to 90 $\mu$M with a detection limit of 0.28 $\mu$M and a sensitivity of 3.98 $\mu A\ \mu M^{-1}\ cm^{-2}$. The sensor also showed reproducible results with good selectivity.

## EXPERIMENTAL SECTION

**Materials.** All chemicals of analytical grade were obtained from Sigma-Aldrich. The aqueous solutions were prepared by using double-distilled (D-D) water. Dimethyl sulfoxide (DMSO) was used for preparing a 1000 $\mu$M stock solution of IMI. A 0.2 M phosphate buffer solution (PBS) was prepared by using disodium hydrogen phosphate and sodium dihydrogen phosphate, by adopting the standard procedures.

**Characterization Techniques.** X-ray diffractograms of the as-prepared sample were collected using a Bruker D8 Advance powder X-ray diffractometer. The phase purity and chemical structure were obtained by employing Raman spectroscopy (Horiba Micro-Raman spectrometer ($\lambda$ = 532 nm, green DPSS laser)). The elemental composition and oxidation states of the surface were analyzed by using X-ray photoelectron spectroscopy (XPS; Kratos, Axis Ultra, UK). Surface area measurements and pore distribution of the sample were analyzed by employing BET measurements (Quantachrome Instruments Nova Touch lx4Model). Morphological studies were carried out by employing an FESEM analysis (Nova Nanosem 450) and TEM analysis (Jeol/JEM 2100). The electrochemical characterizations were performed with the help of a VersaSTAT-3 instrument from Princeton Applied Research, USA. Standard GCE modified with $WS_2$ nanosheets was used as the working electrode, platinum (wire) as the counter electrode, and aqueous Ag/AgCl as the reference electrode. A 0.2 M PBS solution was selected as the supporting electrolyte solution.

**Synthesis of $WS_2$ Nanosheets.** A conventional hydrothermal reaction process was selected for the synthesis of $WS_2$ nanostructures. The hydrothermal preparation of $WS_2$ was noted to be highly sensitive to the reaction temperature. It was reported that reaction temperatures below 240 °C cannot induce the chemical reactions favorable for the formation of $WS_2$.[44] So, a higher reaction temperature of 265 °C was selected for the fabrication of $WS_2$ nanostructures in the present study. The hydrothermal process was carried out by taking tungsten(VI) chloride ($WCl_6$) and thioacetamide (TAA) as primary precursors. A 1.1898 g portion of $WCl_6$ and 1.1269 g of TAA were added to 40 mL of D-D water, and the solution was continuously stirred for 30 min. The obtained solution was moved to a 50 mL PTFE-lined autoclave and was subjected to heating at a temperature of 265 °C for 24 h. After the hydrothermal reaction, a black precipitate was collected. The precipitate was further filtered, washed, and dried in a


https://doi.org/10.1021/acsomega.2c08077
ACS Omega 2023, 8, 8695−8702

vacuum oven at 80 °C. The hydrothermal reaction process for the formation of $WS_2$ is represented by eqs 9 and 10.[45]

$$C_2H_5NS + 2H_2O \rightarrow H_2S + NH_3 + CH_3COOH \quad (9)$$

$$WCl_6 + 3H_2S \rightarrow WS_2 + 6HCl + S \quad (10)$$

When TAA reacts with $H_2O$, $H_2S$ is released. The released $H_2S$ is a strong reducing agent, and it acts as a source of sulfur. This $H_2S$ reduces $WCl_6$ to form $WS_2$ through sulfurization.

**Fabrication of $WS_2$-Modified Glassy-Carbon Electrodes.** Bare GCE was polished and cleaned with 0.3 and 0.05 μm alumina slurries before the actual modification process. Afterward, the electrodes were ultrasonicated in IPA and D-D water to remove the alumina residues. Further, the cleaned electrodes were dried in a hot air oven. A 1 mg portion of an as-prepared powder sample of $WS_2$ was ultrasonicated in 1 mL of a Nafion−ethanol mixture in a ratio of 1:1 for 30 min. A 10 μL portion of the dispersion was drop-casted on the polished and cleaned surface of a GCE and was dried in a vacuum oven at room temperature. A schematic representation of the preparation and fabrication of $WS_2$-modified glassy-carbon electrodes is illustrated in Figure 1.

## AUTHOR INFORMATION


### Corresponding Authors

**S. R. Sarath Kumar** − *Department of Nanoscience and Nanotechnology, University of Kerala, Thiruvananthapuram 695581, India*; Email: sarath.sr.nair@gmail.com

**R. B. Rakhi** − *Materials Science and Technology Division, CSIR-National Institute of Interdisciplinary Sciences (CSIR-NIIST), Thiruvananthapuram, Kerala 695019, India*; Email: rakhiraghavanbaby@niist.res.in

### Author

**V. S. Haritha** − *Department of Physics, University of Kerala, Thiruvananthapuram 695581, India*

Complete contact information is available at: https://pubs.acs.org/10.1021/acsomega.2c08077


### Author Contributions

The manuscript was written through the contributions of all authors. All authors have approved the final version of the manuscript. V.S.H.: conceptualization, methodology, investigation, and drafting of the article. S.R.S.K.: conceptualization, methodology, investigation, writing-reviewing and editing, validation, and supervision. R.B.R.: conceptualization, methodology, investigation, writing-reviewing and editing, validation, and supervision.

### Notes

The authors declare no competing financial interest.

## ACKNOWLEDGMENTS

The authors acknowledge the instrumental support offered for material characterizations from CLIF University of Kerala, Department of the Optoelectronics University of Kerala, Amrita Center for Nanosciences and Molecular Medicine, and CSIR-NIIST. R.B.R. acknowledges financial support from the IC MAP project (DST/TMD/IC-MAP/2K20/01).

## REFERENCES


(1) Carvalho, F. P. Agriculture, Pesticides, Food Security and Food Safety. *Environ. Sci. Policy* **2006**, *9* (7−8), 685−692.

(2) Nicolopoulou-Stamati, P.; Maipas, S.; Kotampasi, C.; Stamatis, P.; Hens, L. Chemical Pesticides and Human Health: The Urgent Need for a New Concept in Agriculture. *Front. Public Heal.* **2016**, *4* (July), 1−8.

(3) Bass, C.; Denholm, I.; Williamson, M. S.; Nauen, R. The Global Status of Insect Resistance to Neonicotinoid Insecticides. *Pestic. Biochem. Physiol.* **2015**, *121*, 78−87.

(4) Jeschke, P.; Nauen, R.; Schindler, M.; Elbert, A. Overview of the Status and Global Strategy for Neonicotinoids. *J. Agric. Food Chem.* **2011**, *59* (7), 2897−2908.

(5) Lv, Y.; Sun, J.; Qiao, S.; Zhang, M.; Li, J. A Facile, Inexpensive and Green Electrochemical Sensor for Sensitive Detection of Imidacloprid Residue in Rice Using Activated Electrodes. *Anal. Methods* **2021**, *13* (33), 3649−3658.

(6) Bruzaca, E. E. S.; De Oliveira, R. C.; Duarte, M. S. S.; Sousa, C. P.; Morais, S.; Correia, A. N.; De Lima-Neto, P. Electrochemical Sensor Based on Multi-Walled Carbon Nanotubes for Imidacloprid Determination. *Anal. Methods* **2021**, *13* (18), 2124−2136.

(7) Xie, W.; Ju, Y.; Zhang, J.; Yang, Y.; Zeng, Y.; Wang, H.; Li, L. Highly Sensitive and Specific Determination of Imidacloprid Pesticide by a Novel Fe3O4@SiO2@MIPIL Fluorescent Sensor. *Anal. Chim. Acta* **2022**, *1195*, 339449.

(8) Kamyabi, M. A.; Moharramnezhad, M.; Hajari, N. Facile Microwave Route for the Synthesis of CuS/CQDs/g-C3N4NS as a Novel Promising Cathodic Electrochemiluminescence Detection of Imidacloprid. *J. Solid State Electrochem.* **2022**, *26* (5), 1259.

(9) Liu, C.; Wei, X.; Wang, X.; Shi, J.; Chen, Z.; Zhang, H.; Zhang, W.; Zou, X. Ratiometric Electrochemical Analysis on a Flexibly-Fabricated Vibratory Electrode Module for Reliable and Selective Determination of Imidacloprid. *Sensors Actuators, B Chem.* **2021**, *329*, 129228.

(10) Armbrust, K. L.; Peeler, H. B. Effects of Formulation on the Run-off of Imidacloprid from Turf. *Pest Manag. Sci.* **2002**, *58* (7), 702−706.

(11) Palomino-Asencio, L.; García-Hernández, E.; Salazar-Villanueva, M.; Chigo-Anota, E. B12N12 Nanocages with Homonuclear Bonds as a Promising Material in the Removal/Degradation of the Insecticide Imidacloprid. *Phys. E Low-Dimensional Syst. Nanostructures* **2021**, *126*, 114456.

(12) Wood, T. J.; Goulson, D. The Environmental Risks of Neonicotinoid Pesticides: A Review of the Evidence Post 2013. *Environ. Sci. Pollut. Res.* **2017**, *24* (21), 17285−17325.

(13) Douglas, M. R.; Rohr, J. R.; Tooker, J. F. Neonicotinoid Insecticide Travels through a Soil Food Chain, Disrupting Biological Control of Non-Target Pests and Decreasing Soya Bean Yield. *J. Appl. Ecol.* **2015**, *52* (1), 250−260.

(14) Chen, D.; Zhang, Y.; Lv, B.; Liu, Z.; Han, J.; Li, J.; Zhao, Y.; Wu, Y. Dietary Exposure to Neonicotinoid Insecticides and Health Risks in the Chinese General Population through Two Consecutive Total Diet Studies. *Environ. Int.* **2020**, *135*, 105399.

(15) Chang, C. H.; Macintosh, D.; Lemos, B.; Zhang, Q.; Lu, C. Characterization of Daily Dietary Intake and the Health Risk of Neonicotinoid Insecticides for the U.S. Population. *J. Agric. Food Chem.* **2018**, *66* (38), 10097−10105.

(16) Moreira, A. A. G.; De Lima-Neto, P.; Caetano, E. W. S.; Barroso-Neto, I. L.; Freire, V. N. The Vibrational Properties of the Bee-Killer Imidacloprid Insecticide: A Molecular Description. *Spectrochim. Acta - Part A Mol. Biomol. Spectrosc.* **2017**, *185*, 245−255.

(17) Vestri, A.; Rippa, M.; Marchesano, V.; Sagnelli, D.; Margheri, G.; Zhou, J.; Petti, L. LSPR Immuno-Sensing Based on Iso-Y Nanopillars for Highly Sensitive and Specific Imidacloprid Detection. *J. Mater. Chem. B* **2021**, *9* (44), 9153−9161.

(18) Kamble, B. B.; Ajalkar, B. D.; Tawade, A. K.; Sharma, K. K.; Mali, S. S.; Hong, C. K.; Bathula, C.; Kadam, A. N.; Tayade, S. N. Ionic Liquid Assisted Synthesis of H-MoO3 Hollow Microrods and Their Application for Electrochemical Sensing of Imidacloprid Pesticide in Vegetables. *J. Mol. Liq.* **2021**, *324*, 115119.

(19) Zhangsun, H.; Wang, Q.; Xu, Z.; Wang, J.; Wang, X.; Zhao, Y.; Zhang, H.; Zhao, S.; Li, L.; Li, Z.; Wang, L. NiCu Nanoalloy

Embedded in N-Doped Porous Carbon Composite as Superior Electrochemical Sensor for Neonicotinoid Determination. *Food Chem.* **2022**, *384*, 132607.
(20) Cho, I. H.; Kim, D. H.; Park, S. Electrochemical Biosensors: Perspective on Functional Nanomaterials for on-Site Analysis. *Biomater. Res.* **2020**, *24* (1), 1−12.
(21) Sandulescu, R.; Tertis, M.; Cristea, C.; Bodoki, E. New Materials for the Construction of Electrochemical Biosensors. *Biosens. - Micro Nanoscale Appl.* **2015**, 1−36.
(22) Zhu, C.; Yang, G.; Li, H.; Du, D.; Lin, Y. Electrochemical Sensors and Biosensors Based on Nanomaterials and Nanostructures. *Anal. Chem.* **2015**, *87* (1), 230−249.
(23) Varghese, S. S.; Varghese, S. H.; Swaminathan, S.; Singh, K. K.; Mittal, V. Two-Dimensional Materials for Sensing: Graphene and Beyond. *Electron.* **2015**, *4* (3), 651−687.
(24) Vargas-Bernal, R. Electrical Properties of Two-Dimensional Materials Used in Gas Sensors. *Sensors (Switzerland)* **2019**, *19* (6), 1295.
(25) Urbanová, V.; Bakandritsos, A.; Jakubec, P.; Szambó, T.; Zbořil, R. A Facile Graphene Oxide Based Sensor for Electrochemical Detection of Neonicotinoids. *Biosens. Bioelectron.* **2017**, *89*, 532−537.
(26) Srinivasan, S.; Nesakumar, N.; Rayappan, J. B. B.; Kulandaiswamy, A. J. Electrochemical Detection of Imidacloprid Using Cu-RGO Composite Nanofibers Modified Glassy Carbon Electrode. *Bull. Environ. Contam. Toxicol.* **2020**, *104* (4), 449−454.
(27) Majidi, M. R.; Ghaderi, S. Facile Fabrication and Characterization of Silver Nanodendrimers Supported by Graphene Nanosheets: A Sensor for Sensitive Electrochemical Determination of Imidacloprid. *J. Electroanal. Chem.* **2017**, *792*, 46−53.
(28) Tawade, A. K.; Mohan Kumar, D.; Talele, P.; Sharma, K. K. K.; Tayade, S. N. Flower-Like ZnO-Decorated Polyaniline-Graphene Oxide Nanocomposite for Electrochemical Oxidation of Imidacloprid: A Hybrid Nanocomposite Sensor. *J. Electron. Mater.* **2019**, *48* (12), 7747−7755.
(29) Han, S. A.; Bhatia, R.; Kim, S. W. Synthesis, Properties and Potential Applications of Two-Dimensional Transition Metal Dichalcogenides. *Nano Converg.* **2015**, *2* (1), 1−14.
(30) Wu, L.; Van Hoof, A. J. F.; Dzade, N. Y.; Gao, L.; Richard, M. I.; Friedrich, H.; De Leeuw, N. H.; Hensen, E. J. M.; Hofmann, J. P. Enhancing the Electrocatalytic Activity of 2H-WS2 for Hydrogen Evolution: Via Defect Engineering. *Phys. Chem. Chem. Phys.* **2019**, *21* (11), 6071−6079.
(31) Haritha, V. S.; Manuraj, M.; Sruthi, T. V.; Kumar, V. B. S.; Kumar, S. A. R. N. S.; Shankar, S. S.; Rakhi, R. B. 3D-Architectured MoS2-Microflower-Modified Electrodes toward Electrochemical Determination of Imidacloprid. *ChemistrySelect* **2022**, *7* (10), e202103362.
(32) Thiehmed, Z.; Shakoor, A.; Altahtamouni, T. Recent Advances in Ws2 and Its Based Heterostructures for Water-Splitting Applications. *Catalysts* **2021**, *11* (11), 1283.
(33) Sun, C.-B.; Zhong, Y.-W.; Fu, W.-J.; Zhao, Z.-Q.; Liu, J.; Ding, J.; Han, X.-P.; Deng, Y.-D.; Hu, W.-B.; Zhong, C. Tungsten Disulfide-Based Nanomaterials for Energy Conversion and Storage. *Tungsten* **2020**, *2* (2), 109−133.
(34) Guo, D.; Cai, K.; Deng, P.; Si, G.; Sun, L.; Chen, F.; Ning, H.; Jin, L.; Ma, J. Structure Tailorable Triple-Phase and Pure Double-Polar-Phase Flexible IF-WS2@poly(Vinylidene Fluoride) Nanocomposites with Enhanced Electrical and Mechanical Properties. *J. Mater.* **2020**, *6* (3), 563−572.
(35) Zeng, H.; Liu, G.-B.; Dai, J.; Yan, Y.; Zhu, B.; He, R.; Xie, L.; Xu, S.; Chen, X.; Yao, W.; Cui, X. Optical Signature of Symmetry Variations and Spin-Valley Coupling in Atomically Thin Tungsten Dichalcogenides. *Sci. Rep.* **2013**, *3*, 2−6.
(36) Mohan, V. V.; Manuraj, M.; Anjana, P. M.; Rakhi, R. B. WS2 Nanoflowers as Efficient Electrode Materials for Supercapacitors. *Energy Technol.* **2022**, *10*, 2100976.
(37) Govindasamy, M.; Wang, S. F.; Jothiramalingam, R.; Noora Ibrahim, S.; Al-lohedan, H. A. A Screen-Printed Electrode Modified with Tungsten Disulfide Nanosheets for Nanomolar Detection of the Arsenic Drug Roxarsone. *Microchim. Acta* **2019**, *186* (7), 420.
(38) Fourmond, V.; Léger, C. *An Introduction to Electrochemical Methods for the Functional Analysis of Metalloproteins* **2020**, 325.
(39) Lei, W.; Wu, Q.; Si, W.; Gu, Z.; Zhang, Y.; Deng, J.; Hao, Q. Electrochemical Determination of Imidacloprid Using Poly-(Carbazole)/ Chemically Reduced Graphene Oxide Modified Glassy Carbon Electrode. *Sensors Actuators, B Chem.* **2013**, *183* (2013), 102−109.
(40) Lei, W.; Han, Z.; Si, W.; Hao, Q.; Zhang, Y.; Xia, M.; Wang, F. Sensitive and Selective Detection of Imidacloprid by Graphene-Oxide-Modified Glassy Carbon Electrode. *ChemElectroChem.* **2014**, *1* (6), 1063−1067.
(41) Si, W.; Han, Z.; Lei, W.; Wu, Q.; Zhang, Y.; Xia, M.; Hao, Q. Fast Electrochemical Determination of Imidacloprid at an Activated Glassy Carbon Electrode. *J. Electrochem. Soc.* **2014**, *161* (1), B9−B13.
(42) Kong, L.; Jiang, X.; Zeng, Y.; Zhou, T.; Shi, G. Molecularly Imprinted Sensor Based on Electropolmerized Poly(o-Phenylenediamine) Membranes at Reduced Graphene Oxide Modified Electrode for Imidacloprid Determination. *Sensors Actuators, B Chem.* **2013**, *185*, 424−431.
(43) Paula, S. A.; Ferreira, O. A. E.; César, P. A. Determination of Imidacloprid Based on the Development of a Glassy Carbon Electrode Modified with Reduced Graphene Oxide and Manganese (II) Phthalocyanine. *Electroanalysis* **2020**, *32* (1), 86−94.
(44) Shang, Y.; Xia, J.; Xu, Z.; Chen, W. Hydrothermal Synthesis and Characterization of Quasi-1-D Tungsten Disulfide Nanocrystal. *J. Dispers. Sci. Technol.* **2005**, *26* (5), 635−639.
(45) Yang, J.; Voiry, D.; Ahn, S. J.; Kang, D.; Kim, A. Y.; Chhowalla, M.; Shin, H. S. Two-Dimensional Hybrid Nanosheets of Tungsten Disulfide and Reduced Graphene Oxide as Catalysts for Enhanced Hydrogen Evolution. *Angew. Chem.* **2013**, *125* (51), 13996−13999.


https://doi.org/10.1021/acsomega.2c08077
*ACS Omega* 2023, 8, 8695−8702